Journal of Crystal Growth 602 (2023) 126943

Contents lists available at ScienceDirect

Journal of Crystal Growth

journal homepage: www.elsevier.com/locate/jcrysgro

Gel-mediated chemo-mechanical control of calcium carbonate crystal formation

Damian Palin [a,b,c,*], Jennie A.M.R. Kunitake [a], Marina P. Chang [a], Stephan Sutter [a], Lara A. Estroff [a,d,*]

[a] Department of Materials Science and Engineering, Cornell University, Ithaca, NY 14853, United States
[b] Department 3MD Faculty of Civil and Engineering and Geosciences, Delft University of Technology, 2628 CN Delft, the Netherlands
[c] Department of Engineering, University of Cambridge, Trumpington Street, Cambridge CB2 1PZ, United Kingdom
[d] Kavli Institute at Cornell for Nanoscale Science, Cornell University, Ithaca, NY 14853, United States

ARTICLE INFO

Communicated by James J. De Yoreo

Keywords:
A1. Crystal morphology
A1. Biocrystallization
A1. Impurities
A2. Growth from solution
B1. Calcium compounds
B1. Minerals

ABSTRACT

The production of synthetic crystals with controlled shapes and properties is an enticing prospect, yet, the production of such materials is an ongoing challenge. Here, we present a strategy for chemo-mechanically directing the growth of crystals with non-equilibrium structures using a custom-designed double-diffusion cell. We combine chemical additives (e.g., Mg^{2+} ions) and mechanical confinement (e.g., hydrogel networks) to modulate the growth of calcium carbonate crystals. Specifically, the combination of Mg^{2+} ions with a strong agarose gel results in calcitic structures, at the gel-glass slide interface, with distinct fried egg-like morphologies and radial or Maltese-cross extinction patterns. In contrast, precipitation with only Mg^{2+} or agarose results in aragonite spherulites or squished calcite rhombohedra, respectively. Raman spectroscopy and energy dispersive spectroscopy of the "fried eggs" reveals that they are composed of Mg-calcite, which becomes less disordered over time, and the "egg whites" make this transition before the "yolks". We propose that the "fried eggs" form due to a spherulitic growth process molded by the crystallization-induced delamination of the gel away from the glass slide at the gel-glass interface. In support of the importance of the gel-glass interface, the "fried eggs" do not form when the glass slide is treated with a hydrophobic silane, suppressing heterogeneous nucleation and weakening the interfacial adhesion between the gel and glass, making it easier for the gel to delaminate, thus reducing the confinement effect. As such, this work highlights the important chemo-mechanical role that gel environments can play in crystal formation.

1. Introduction

Nature exerts exquisite control over her biomineralized tissues. The formation of these tissues is intimately associated with organic extracellular matrices that chemically modulate and mechanically "mold" the inorganic mineral phases [1–6]. Specific charged molecules or ions within organic matrices can stabilize amorphous phases before crystallization [1,2,7], allowing rapid yet fine control over phase selection, shape, and structure [7]. The resulting composite tissues can display outstanding mechanical [3–6,8] and optical [6,9,10] properties related to their specific functions. Therefore, understanding the chemo-mechanical processes involved in matrix-mediated crystal formation can provide insights into biomineralization and design strategies for synthesizing crystalline materials with advanced functional properties.

Scientists fascinated by biomineralized tissues have long sought to understand and replicate their formation [11,12]. Experiments have demonstrated how inorganic and organic additives influence crystal habits in solution [13–24]. Magnesium, for example, strongly inhibits the formation of calcite (the thermodynamically stable polymorph of calcium carbonate at ambient temperatures and pressures) [15–17,19,20,22–24]. At Mg^{2+}/Ca^{2+} ratios equal to or greater than 4, aragonite (a metastable polymorph of calcium carbonate) forms with acicular spheroidal or cauliflower-like morphologies [15,16]. While at ratios of <1 to 4, Mg-calcite ($[Ca, Mg]CO_3$) spherulites (polycrystalline aggregates of anisometric or radiating crystals with an outer spherical envelope [25–27]) [17,19,20,23] or films of intergrown spheres [22]

* Corresponding authors at: Department of Engineering, University of Cambridge, Trumpington Street, Cambridge CB2 1PZ, United Kingdom (D. Palin). Department of Materials Science and Engineering, Cornell University, Ithaca, NY 14853, United States (L.A. Estroff).
E-mail addresses: dp673@cam.ac.uk (D. Palin), lae37@cornell.edu (L.A. Estroff).

https://doi.org/10.1016/j.jcrysgro.2022.126943
Received 2 June 2022; Received in revised form 1 October 2022; Accepted 14 October 2022
Available online 19 October 2022

can form. The physical basis for the influence of Mg^{2+} on calcium carbonate mineralization is a topic of ongoing debate. Studies suggest that Mg^{2+} inhibits calcite formation in solutions with high Mg^{2+}/Ca^{2+} ratios due to the adsorption of Mg^{2+} onto the surface of nascent crystals, thus blocking growth sites [16,28,29]. Others suggest that Mg^{2+} is incorporated into the calcite lattice, increasing its solubility [30,31]. Aragonite forms at higher Mg^{2+} concentrations as it is relatively uninhibited by Mg^{2+} [16]. The basis for the formation of Mg-calcite spherulites is also debated. Some suggest that Mg^{2+} incorporation introduces lattice strains and small-angle grain boundaries leading to "split growth" [32]. Others propose that Mg^{2+} stabilizes amorphous calcium carbonate (ACC, a metastable phase), which forms into spheres to minimize surface contact with its surroundings [20], and converts to Mg-calcite spherulites under specific solution conditions [19,20,23].

Experiments have also shown that confinement using rigid three-dimensional templates can mechanically govern crystal morphology [33,34] and polymorph selectivity [35]. For example, when calcite [33] and aragonite [34] are grown within micro-cylindrical pores, the resulting crystals have rod-like shapes, which are defined by the pores and not observed in bulk solution. The non-equilibrium rod-like morphologies result from mechanical "molding" of the crystals via confinement within the pores. Furthermore, precipitation of calcium carbonate between crossed-cylinders stabilizes ACC over calcite [35]. The surface free energy of ACC is expected to be lower than calcite under such conditions due to the increased surface area to volume ratio of ACC particles.

Inspired by the mineralized organic matrices of organisms, crystal growth in gels has emerged as a powerful synthetic platform for modeling and understanding biogenic crystal formation [36]. Gels provide a diffusion-limited environment, which influences crystal habit. For example, calcite crystals grown in agarose, a hydrophilic, uncharged gel, can have equilibrium rhombohedra to hopper-like or skeletal-shaped morphologies [36,37]. As with the solution studies above, gel studies have shown that crystal habit can be controlled by introducing inorganic and organic additives to the gel matrix [32,38–44]. For example, studies in which Mg^{2+} was added to gels demonstrated that a range of structures can form, including single crystal high-Mg calcite and polycrystalline Mg-calcite spherulites [32,39,44]. Other studies have shown that gel networks can mechanically modulate crystal habit [36,37,45]. By growing calcite crystals in agarose gels, researchers demonstrated that the gel-grown crystals occlude gel fibers, resulting in single crystal composites [36,37,45]. Inspired by the seminal work of Chernov and co-workers [14,46], the researchers demonstrated that this gel occlusion only occurs if the gel is strong enough to resist the crystallization pressure, which is related to the supersaturation, and at a critical crystal growth rate [36,37]. Recently researchers also demonstrated that calcite crystals grown in anisotropically structured agarose gels fracture these gels parallel to their fiber structure and that the fractures "mold" the crystals, yielding anisotropically shaped crystal composites [45].

Although the studies above have provided insights into the chemical *or* mechanical roles gel environments can play in crystal formation, the combined chemo-mechanical impact of these mechanisms is not well understood. To shed light on this subject, we present a strategy to investigate the combined influence of chemical additives (e.g., Mg^{2+}) and mechanical confinement (e.g., hydrogels of varying physical strength) by growing calcium carbonate in a custom-built double-diffusion reactor. We characterize the structure and composition of the resulting crystals and suggest a possible model describing their formation.

2. Experimental design

To investigate the chemo-mechanical influence of gel environments on crystal formation, we custom-designed a double-diffusion cell in which a thin gel film (~2 × 25 × 25 mm) is sandwiched between two glass slides, which we sealed down two sides (Fig. 1, left). This diffusion cell is then secured between two reservoirs containing the desired cationic and anionic components (Fig. 1, right). In this system, where the crystals are forced to grow within the gel, the mechanical confinement comes both at the nanoscale via the gel fiber structure and at the millimeter scale via the thin gel film confined between two slides. In addition, chemical additives can be introduced into this system via diffusion. Specifically, we precipitated calcium carbonate in cells containing agarose gels of varying strengths, in order of increasing strength: i) agarose Type IX 3% w/v (AIX3; which has a storage modulus, G′, of 0.01 MPa and a maximum loss modulus, G''_{max}, of 0.002 MPa (Fig. S1a); ii) agarose Type IB 3% w/v (AIB3; which has a G′ of 0.1 MPa and G''_{max} of 0.02 MPa (Fig. S1b); and iii) agarose Type IB 4% w/v (AIB4). These gels were placed into the double-diffusion setup with a solution of 50 mM $CaCl_2$ and 200 mM $MgCl_2$ (Mg^{2+}/Ca^{2+} ratio of 4) in the outer reservoir and a solution of 50 mM $NaHCO_3$ in the inner reservoir. As controls, we also precipitated calcium carbonate in diffusion cells containing: no Mg^{2+} and no gel; no Mg^{2+} and gels of different strengths (AIX3, AIB3, AIB4). We then monitored the structure of the resultant crystals via light microscopy, plane-polarized light microscopy, and scanning electron microscopy (SEM), their crystal phase via Raman microspectroscopy, and their elemental composition via energy dispersive spectroscopy (EDS). Finally, to evaluate the role of the glass slide as a heterogeneous nucleating surface, we constructed diffusion cells with hydrophobic, octadecyltrichlorosilane (OTS)-treated glass slides.

3. Results

3.1. Crystal characteristics

Calcium carbonate crystals were grown for 14 days in eight different conditions (in solution and three gel types, each with and without Mg^{2+}). Plane-polarized light microscopy shows that the crystals formed in the bulk gel have morphologies consistent with previous reports of gel-grown calcite [32,37,39,44,45], in contrast to those formed at the gel-glass interface, which have distinct morphologies (Fig. S2a,c). For example, crystals formed within the AIB3 gel with no Mg^{2+} have hopper-like morphologies (Fig. S2b (black arrow)), and the crystals formed in the AIB3 gel with Mg^{2+} have spheroidal or dumbbell morphologies (Fig. S2d (black arrow)). Since crystals with hopper-like [36,37] and spheroidal [32,39,44] morphologies are known to form in gels containing no Mg^{2+} and Mg^{2+}, respectively, we decided to focus on the crystals formed at the gel-glass interface. The crystals formed at the gel-glass interface display different morphological, optical, and chemical characteristics depending on the specific growth conditions (Table 1). In the four control conditions without any Mg^{2+}, calcite was the majority phase, as determined by Raman microspectroscopy, having characteristic peaks occurring at ~1085 cm^{-1} (ν_1, the carbonate symmetric stretching mode), ~710 cm^{-1} (ν_4, the carbonate in-plane bending mode) and lattice modes at ~280 and 155 cm^{-1} (Fig. S3, center) [47–49]. Plane-polarized light microscopy analysis of these crystals showed an evolution in the morphology of the crystals from equilibrium calcite rhombohedral morphologies in the absence of gel (Fig. 2a,e and Fig. S3a) to "knobbled" rhombohedra-like morphologies in the AIX3 (mechanically weak) gel (Fig. 2b,f and Fig. S3b) to "squished" rhombohedral morphologies in the AIB3 (mechanically strong, lower weight percentage) gel (Fig. 2c,g and Fig. S3c) and finally thin plate-like morphologies with rhombohedral features in the AIB4 (mechanically strong, higher weight percentage) gel (Fig. 2d,h and Fig. S3e). In AIB4, the crystals begin to impinge on each other, forming tessellated polygonal macrostructures. In all of these cases, the crystals, when viewed through crossed-polarizers, "blink" when rotated, indicating single crystal domains (Fig. 2e-h).

When a chemical additive (Mg^{2+}) is added to the outer reservoir together with Ca^{2+}, the compositions and morphologies of the resulting crystals undergo substantial changes. Specifically, in the absence of any

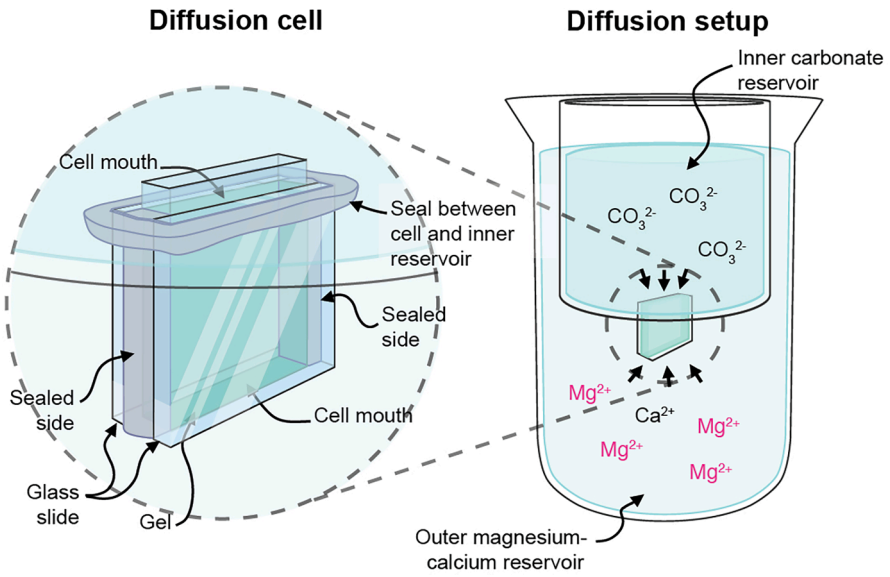

Fig. 1. Schematic illustrations of: (Left) the diffusion cell; and (Right) the solution-based double-diffusion setup used to precipitate calcium carbonate crystals in the diffusion cells.

Table 1
Summary of the precipitation experiments and the resulting crystal characteristics.

Gel[1]	Mg^{2+}/Ca^{2+}	Morphology[2]	Optical character[3]	Crystal Phase[4]
None	0	Rhombohedra	Blink	Calcite[(a)]
AIX3	0	Knobbled rhombohedra	Blink	Calcite[(b)]
AIB3	0	Squished rhombohedra	Blink	Calcite[(c)]
		Rounded rhombohedra	Dull blink	Monohydrocalcite[(d)]
AIB4	0	Plates	Blink	Calcite[(e)]
None	4	Spherulites	Dull constant extinctions	Aragonite[(f)]
AIX3	4	Spherulites	Dull constant extinctions	Aragonite[(g,h)]
AIB3	4	Fried egg-like	Maltese-cross	Calcite[(i)]
		Spherulites	Dull constant extinctions	Aragonite[(j)]
		Lemon-like	Dull blink	Monohydrocalcite[(k)]
AIB4	4	Fried egg-like	Maltese-cross	Calcite[(l)]
		Spherulites	Dull constant extinctions	Aragonite[(m)]

[1]AIX3 = Agarose IX, 3% w/v. AIB3 = Agarose IB, 3% w/v. AIB4 = Agarose IB, 4% w/v. [2]Crystal morphology was assessed by light microscopy. [3]Crystal optical character was assessed by rotating the crystals when viewed by light microscopy through crossed-polarizers. [4]Crystal phase was established using Raman spectroscopy (the superscript letters (a–m) in parenthesis correspond to the images and spectra in Fig. S3).

gel and the presence of the weakest gel (AIX3), the precipitates have spheroidal and cauliflower-like morphologies (Fig. 2i,j,m,n and Fig. S3f, g,h). Raman microspectroscopy identifies these structures as aragonite with peaks situated just under 1085 cm^{-1} (ν_1) and at ~702 cm^{-1} (ν_4), and prominent lattice modes occurring at ~206 and 152 cm^{-1} (Fig. S3, center) [47]. When viewed through crossed-polarizers, the spheroidal and cauliflower-like structures have continuous dull extinctions (Fig. 2m,n).

As the gel strength increases (AIB3 and AIB4), there is a distinct change in the morphology of the precipitates formed in the presence of Mg^{2+}. In the AIB3 gel, the majority of the structures are reminiscent of a fried egg (i.e., there is a hemispherical region in their center that looks like a fried egg yolk surrounded by a flatter region that looks like a fried egg white, with average total diameters of 250 μm), and are well-spaced with some impinging on each other (Fig. 2k,o, Fig. S3i and Fig. S4 (pink arrows)). Often a groove can be seen across the "fried egg" crystals, almost separating them into two halves (Fig. 2k (pink arrow)). In the AIB4 gels, similar "fried egg" morphologies are observed, which are smaller (150 μm) than those in AIB3 and more densely packed with many impinging on each other, forming tessellated polygonal macrostructures (Fig. 2l,p), as well as some crystals with spheroidal morphologies (Fig. S3m). Significantly, despite their morphology, the "fried egg" crystals have Raman spectra consistent with calcite (Fig. S3i,l, center). Furthermore, when viewed between crossed-polarizers, the "fried eggs" display distinctive radial or Maltese-cross extinction patterns consistent with spherulitic growth (Fig. 2o,p). In addition to the "fried eggs", there are a small number of crystals with spheroidal morphologies (Fig. S3j and Fig. S4c (white arrows)) and, in rare cases, lemon-like morphologies (Fig. S3k). The lemon-shaped crystals observed in the AIB3 gel are monohydrocalcite, with a peak at ~1066 cm^{-1} (ν_1) and two bands at ~700 and 723 cm^{-1} (ν_4, Fig. S3k, center) [50]. The crystals with the "fried egg" morphologies form closer to the Mg^{2+}/Ca^{2+} reservoir, while the spherulites form closer to the carbonate reservoir (Fig. S4). Furthermore, among the growth environments containing Mg^{2+}, comparing crystals with fried egg and non-fried egg morphologies formed after 14 days, the ν_1 peaks of the non-fried eggs are significantly broader than the ν_1 peaks of the fried eggs ($p = 0.004$, Fig. S5).

SEM images of the crystals formed in cells containing Mg^{2+} and no gel, no Mg^{2+} and AIB3 gel, and Mg^{2+} and the AIB3 gel confirm their spheroidal (Fig. 3a), squished rhomboid (Fig. 3c), and fried egg-like (Fig. 3e) morphologies, respectively. Higher magnification SEM images of the surface structures of these crystals reveal that the spheroids have the acicular microstructure of aragonite (Fig. 3b). The squished

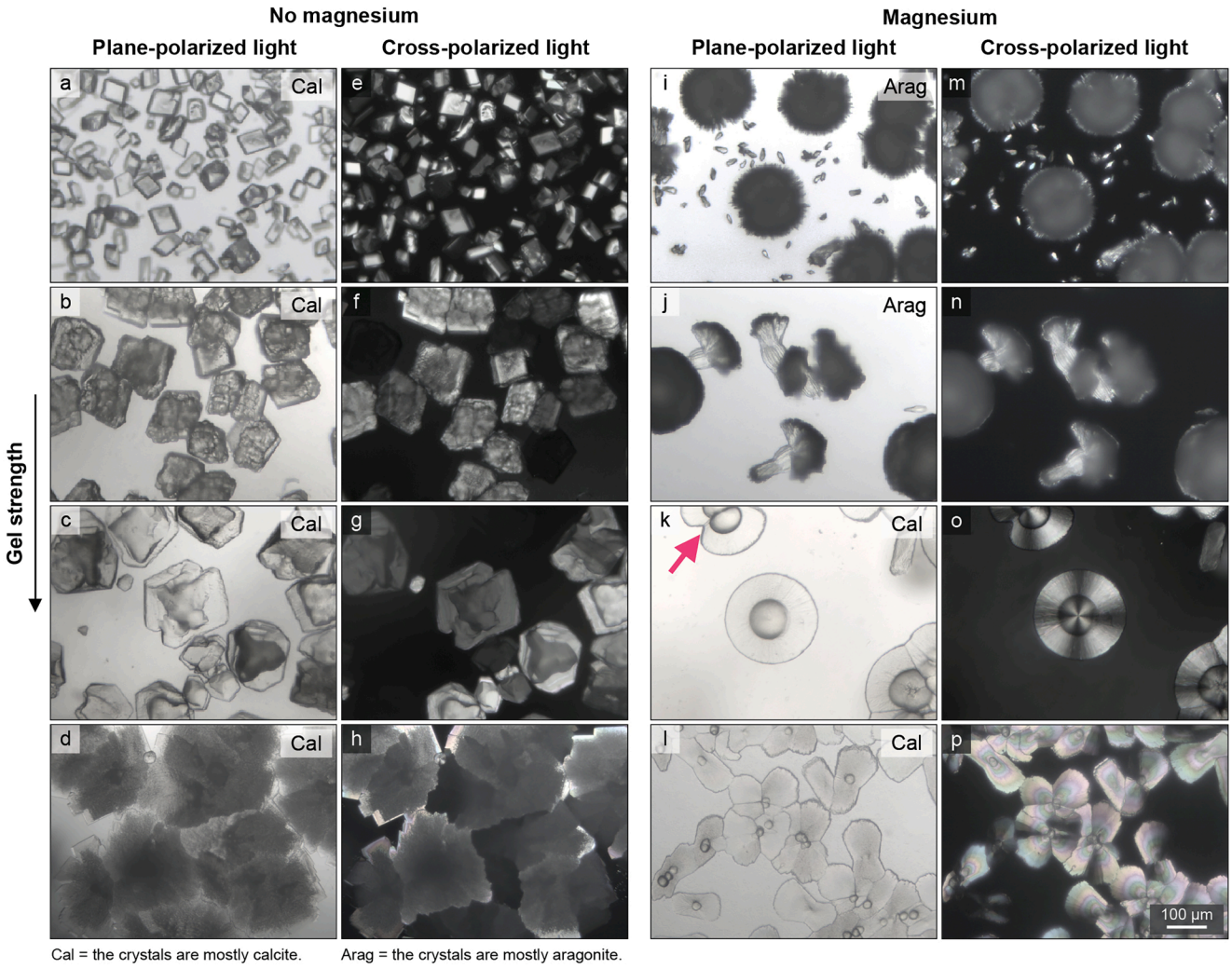

Fig. 2. Polarized light microscope images of calcium carbonate crystallites formed on the surface of the glass slides following 14 days diffusion within cells containing: (a–h) no Mg^{2+} (50 mM $CaCl_2$ with 50 mM $NaHCO_3$); (i–p) Mg^{2+} (50 mM $CaCl_2$ and 200 mM $MgCl_2$ with 50 mM $NaHCO_3$); (a,e,i,m) no gel; (b,f,j,n) agarose IX 3 w/v %; (c,g,k,o) agarose IB 3 w/v %; and (d,h,l,p) agarose IB 4 w/v %. (a–d,i–j) Images taken under plane-polarized light and (e–h,m–p) through crossed-polarizers. The pink arrow in (k) points at a fried egg-like crystal with a groove through its center, almost splitting it in two. Crystal phase was established using Raman microspectroscopy (see Fig. S3).

rhomboids have the highly aligned {104} facets of calcite (Fig. 3d). The fried egg crystals have polycrystalline microstructures, which radiate out from their centers and are terminated at their tips by rhombohedral {104} facets (Fig. 3f (white arrows)).

3.2. *Fried egg-like crystal characteristics over time*

Given the appearance of the unusual, fried egg-like structures, we analyzed them further. Specifically, we analyzed the fried eggs formed in the presence of Mg^{2+} and the AIB3 gel over time using plane-polarized light microscopy, SEM, Raman spectroscopy, and EDS. Plane-polarized light and SEM microscopy images of the crystals show that their morphology evolves with time (Fig. 4a–i). The crystals, after 5 days of growth, have small fried egg (25 µm, Fig. 4a,d,g) and "egg yolk" (i.e., hemispherical; 10 µm, Fig. 4g (white arrows)) morphologies that are well spaced from each other on the glass slides. The crystals formed after 9 days are larger "fried eggs," with some seeming to encroach on each other (50 µm, Fig. 4b,e,h), and after 14 days, they develop into even larger "fried eggs" (as described above, Fig. 2k,o, Fig. 3e and Fig. 4c,f,i). In addition, the crystals viewed through crossed-polarizers display Maltese-cross extinction patterns at 9 and 14 days (Fig. 2o and Fig. 4e,f). Raman spectroscopy of fried eggs shows their ν_1 peak is broader and shifted to a higher energy than calcite formed on glass within Mg-free cells (Fig. 4j). This behavior is consistent with all crystals grown in the presence of Mg^{2+}, no matter the gel type and/or substrate (Fig. S6). The full width at half maximum (FWHM) of the ν_1 peak of crystals formed in cells with Mg^{2+} is significantly increased ($p < 0.0001$) and closer to the value of calcite from *Atrina rigida*, a known biogenic Mg-calcite, as compared to crystals grown without Mg^{2+}, which have FWHMs closer to geological calcite (Fig. S6a). In addition, the average Raman shift of the ν_1 peaks is significantly higher (1087.4 versus 1085.7 cm^{-1}, $p < 0.0001$) for crystals synthesized in the presence of Mg^{2+} versus those not (Fig. S6c). Raman spectra did not provide unequivocal evidence of amorphous calcium carbonate though its presence cannot be ruled out. EDS analysis of fried eggs formed in the presence of Mg^{2+} reveals that they contain both Ca and Mg, while the rhombohedral crystals formed in the presence of no Mg^{2+} contain only Ca (Fig. S8a).

Additional investigation of the fried egg crystals reveals that their structure and composition are different across their bodies and change over time (Fig. 4n). Raman analysis of the fried eggs taken after 5 days of growth, reveals that the ν_1 peaks of the spectra are widest, and the FWHM values are comparable for whites and yolks, with yolk peak widths trending gradually lower over time (Fig. 4n). On analyzing FWHM with a linear mixed-effects model (See section *7.5. Statistical*

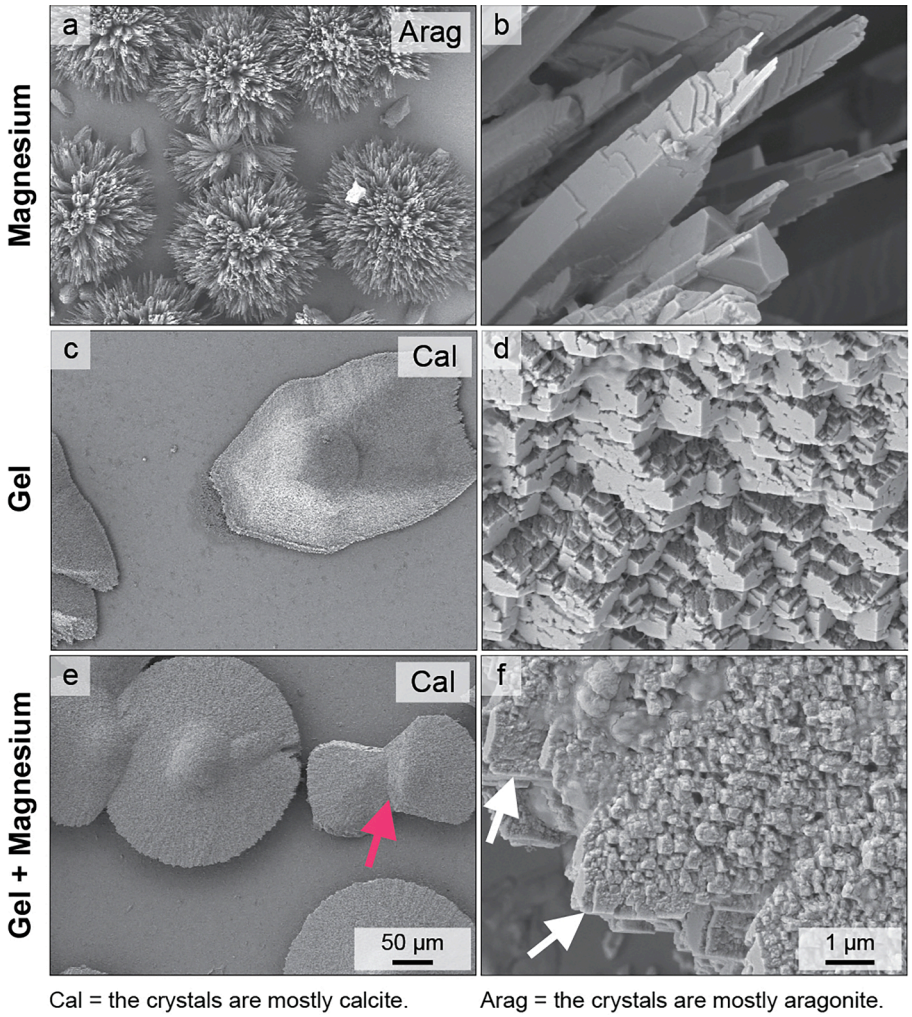

Fig. 3. Representative scanning electron microscope images of crystals formed on the surface of the glass slides following 14 days diffusion within cells containing: (a,b) Mg^{2+} (50 mM $CaCl_2$ and 200 mM $MgCl_2$ with 50 mM $NaHCO_3$) and no gel; (c,d) no Mg^{2+} (50 mM $CaCl_2$ with 50 mM $NaHCO_3$) and gel (agarose IB 3% w/v); and (e,f) Mg^{2+} (50 mM $CaCl_2$ and 200 mM $MgCl_2$ with 50 mM $NaHCO_3$) and gel (agarose IB 3% w/v). Images (a,c,e) show overviews of crystals and (b,d,f) the surface of one of the crystals at a higher magnification. The white arrows in (f) point to the tips of the fried eggs terminated by the {104} facets of calcite. Crystal phase was established using Raman microspectroscopy (see Fig. S3).

analysis, $R^2 = 0.95$), there is a significant interaction ($F_{2,9} = 12.06$, $p = 0.003$) between sampling location (i.e., whites versus yolk) and time (i.e., at 5, 9, or 14 days growth). In addition, a statistically significant reduction in width is evident between yolks at 5 and 14 days ($p = 0.025$). For whites, the mean peak widths are narrowest after 9 days, with significantly narrower peaks than at day 5 ($p = 0.007$) and a nonsignificant increase after 14 days. Whites and yolks also differ significantly after 9 days ($p = 0.0003$) but not after 5 or 14 days. This behavior is also evident in the peak width trends of individual eggs, with the yolks having broader peaks than whites for 5/5 eggs measured at 9 days (Fig. S7). EDS analysis of fried eggs reveals the presence of Mg^{2+} at all time points in both yolks and whites (Fig. S8a) and no qualitative differences between whites and yolks within individual eggs (Fig. S8b-d).

3.3. Growth on a hydrophobic surface

To test the importance of the glass slide surface (primarily silanols) in the formation of the observed morphologies, we prepared the diffusion cells as before (i.e., containing Mg^{2+} and AIB3 gel); however, this time, we made the surface of the glass hydrophobic by coating it with OTS. Compared to the native hydrophilic silanols, OTS-coated glass is known to prevent crystal nucleation and eliminate possible hydrogen bonding sites [51]. Precipitation of calcium carbonate within these cells resulted in aragonite spherulites, not calcite "fried eggs" (Fig. 5 and Fig. S3o).

4. Discussion

We employed Mg^{2+} (the chemical component of the system) and agarose gels with varied mechanical strengths (the mechanical component of the system) to chemo-mechanically control calcium carbonate formation. The growth of calcium carbonate in the cells in the presence of Mg^{2+} and strong gels yielded Mg-calcite crystals (Fig. S8) with distinct fried egg-like morphologies (Fig. 2k,l,o,p, Fig. 3e, Fig. 4b,c,e,f, g–i, Fig. S3i,l, Fig. S4c (pink arrows)), and familiar structural characteristics (Fig. 2k (pink arrow),l,o,p, and Fig. 4b,c,e,f,h). Calcium carbonate structures with fried egg-like morphologies formed within synthetic models of nacre consisting of a peptide (n16N), silk fibroin, and β-chitin [42] and rPif80 and β-chitin; [52] in these instances, the authors reported that these crystals were composed of vaterite (a metastable form of calcium carbonate) and ACC [42] and polymer-induced liquid precursor-like amorphous calcium carbonate granules [52] and proposed no model for the formation of the observed shapes.

The growth of calcium carbonate in the presence of Mg^{2+} containing no gel or low-strength gels resulted in aragonite spherulites (Fig. 2i,j,m, n, Fig. 3a,b, and Fig. S3f–h), consistent with the literature [15,16]. In the absence of Mg^{2+} and the presence of gels with increasing gel strength, the calcite crystals formed at the gel-glass interface became increasingly "squished" while maintaining their characteristic calcite rhombohedral character (Fig. 2a–h, Fig. 3c,d, and Fig. S3a–c,e). This change in shape is consistent with previous experiments in which calcium carbonate crystals were grown confined between crossed cylinders [35]. The "squishing" suggests that the stronger agarose gels provide the crystals with

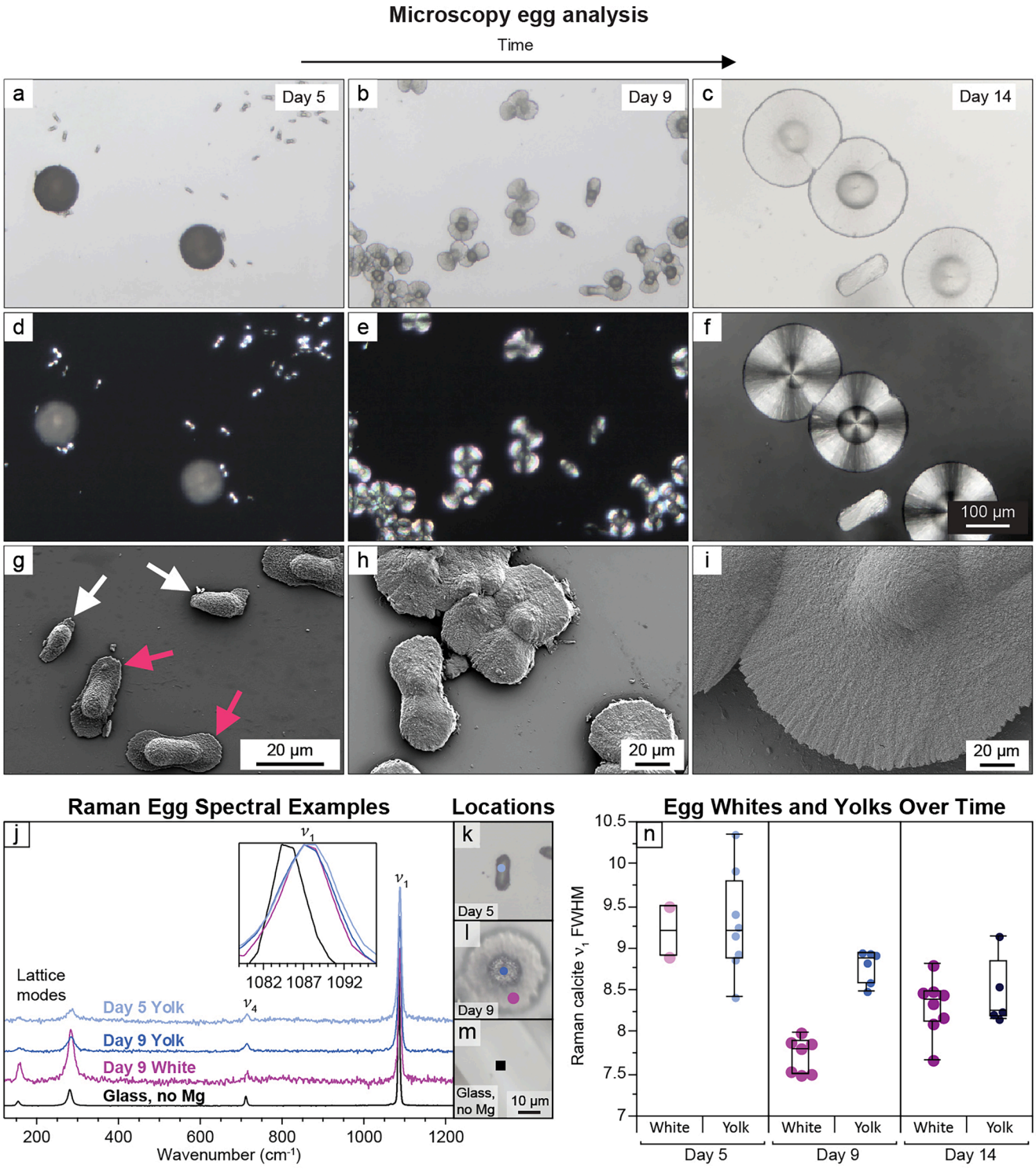

Fig. 4. Analysis of the crystals formed over time in the presence of Mg^{2+} (50 mM $CaCl_2$ and 200 mM $MgCl_2$ with 50 mM $NaHCO_3$) and agarose IB 3% w/v: (a–i) representative images of crystals taken after 5, 9, and 14 days using (a–c) light microscopy under plane-polarized light, and (d–f) through crossed-polarizers, and (g–i) scanning electron microscopy; (j) representative Raman spectra of an "egg yolk" after 5 and 9 days, an "egg white" after 9 days, and a calcite crystal grown in a cell containing no magnesium and no gel after 14 days. Calcite peaks are labeled lattice modes, ν_1, and ν_4, corresponding to the calcite lattice, and the symmetric stretching and in-plane bending vibrational modes of carbonate in calcite, respectively. The inset shows an expanded plot of the ν_1 band (spectra have been normalized to the ν_1 peak); (k–m) light microscopy images of the crystals showing the locations where the spectra were taken; (n) a plot of the ν_1 FWHM from "egg yolks" and "egg whites" over time. The white and pink arrows in (g) point to egg yolks and egg whites, respectively. For (n), a linear mixed-effects model was used to analyze the FWHM (See section *7.5. Statistical analysis*, $R^2 = 0.95$). There was a significant interaction between location and time ($F_{2,9} = 12.06$, $p = 0.003$). Statistically significant differences (using Tukey's honestly significant difference test) were found for whites on day 5 versus day 9 ($p = 0.007$), yolks on day 5 versus day 14 ($p = 0.025$), and day 9 whites versus day 9 yolks ($p = 0.0003$). (For interpretation of the references to colour in this figure legend, the reader is referred to the web version of this article.)

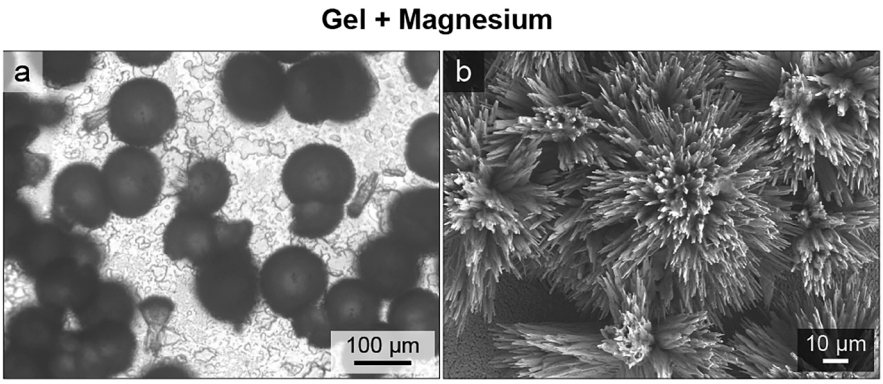

Fig. 5. Analysis of crystals formed within cells constructed from OTS-coated glass slides sandwiching agarose IB 3% w/v following 14 days diffusion (50 mM $CaCl_2$ and 200 mM $MgCl_2$ with 50 mM $NaHCO_3$) using: (a) light microscopy and; (b) scanning electron microscopy.

enough resistance that they grow preferentially along the gel-glass interface rather than into the gel.

The Maltese-cross extinction patterns of the "fried eggs" are characteristic of spherulites [27]. Spherulites generally form via non-crystallographic branching or "split growth," whereby a parent crystal nucleates crystallographically independent daughter crystals [25–27]. Magnesium ions in solution [17,19,20,23] and gels [32,39,44] promote calcite spherulite formation. Authors have attributed the formation of calcite spherulites to misfit lattice strains associated with Mg^{2+} incorporation [32]. Spherulites, as they form, can pass through intermediate sheaf-of-wheat and dumbbell-like morphologies that grow back onto themselves, resulting in spherical crystals with equatorial grooves [19]. Our "fried eggs", despite their unusual shape, often display grooves across their bodies (Fig. 2k (pink arrow), and Fig. 4b,h), consistent with a non-crystallographic branching or split growth process. Researchers have also shown that calcite spherulites form in the presence of Mg^{2+} ions via amorphous precursor phases [17,19,20,23,24]. The amorphous phase takes the shape of a sphere, as expected for a liquid phase that wants to minimize its surface contact with its surroundings [20].

The shape of the "fried eggs" is curious and reminiscent of the shape of calcite composite discs formed in anisotropically structured gels [45]. In that work, the authors proposed that calcite crystals grown within anisotropically structured gels exerted a crystallization pressure that fractured the gel parallel to the oriented network resulting in the growth of calcite disks molded by the fractures. They further proposed that the disks, as they formed, occluded those parts of the network that were strong enough to resist the crystallization pressure. A similar mechanism is potentially at play in the formation of the fried eggs. The crystals, as they grow, exert a crystallization pressure which, in a kind of fracture, pushes the compliant gel away from the stiff glass slide (disrupting hydrogen bonds between the agarose hydroxyl groups and the surface silanols), generating anisotropic interstitial spaces into which the egg whites grow (Fig. 4g (pink arrows)). As the fried eggs form, they too likely occlude those parts of the gel network that are strong enough to resist the crystallization pressure while the weaker parts are pushed away and build up at the crystallization front. This confinement mechanism can also explain the "squished" calcite crystals observed in the strongest gel containing no magnesium (Fig. 2d,h). Further confirmation of the importance of growth at the gel-glass interface comes from the experiments with OTS-coated glass slides. In these experiments, the hydrophobic surface suppresses nucleation and weakens the interfacial adhesion at the gel-glass interface, leading to nucleation and growth of aragonite crystals.

The fried egg crystals undergo temporal structural and compositional changes. As the crystals mature, they become more crystalline (i.e., less disordered) over time, with the "whites" undergoing this maturation before the "yolks" (Fig. 4n). This observation is based on the narrowing ν_1 calcite Raman band, capturing a decrease in local disorder. In this experiment, the disorder could be due to many factors, including, but not limited to, magnesium incorporation [53], the presence of amorphous or disordered phases, and/or gel incorporation. The lack of corresponding trends of magnesium content at any time point (Fig. S8b) suggests magnesium alone does not account for the band broadness, and there may be multiple mechanisms behind the observed changes. We do not fully understand the crystals' maturation; however, we suspect that the maturation occurs via dissolution and crystallization [54,55] and/or a solid-state conversion of an amorphous to a crystalline phase [54,56]. As the ion reservoirs are not infinite or semi-infinite [57] and we know that the Ca^{2+} ions are consumed faster during calcite or aragonite growth than the Mg^{2+} ions, this maturation likely occurs due to

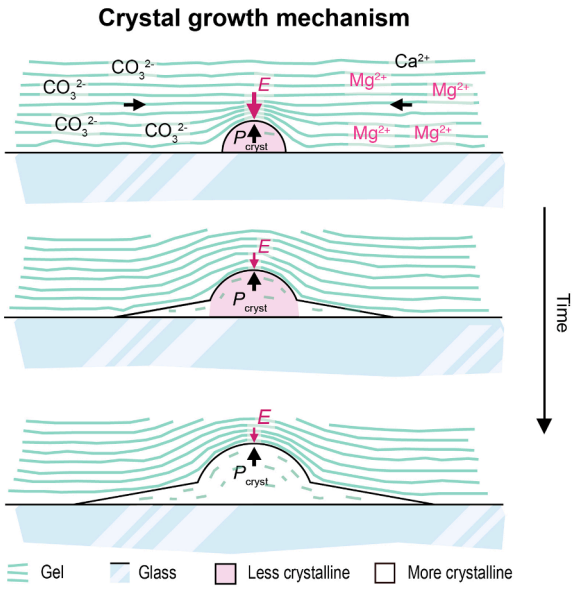

Fig. 6. Schematic representation of a speculative model describing the growth process leading to the formation of the fried egg-shaped crystals within a diffusion cell containing Mg^{2+} and a strong agarose gel: (top) Ca^{2+}, Mg^{2+}, and CO_3^{2-} ions diffuse into the cell. A calcitic phase nucleates on the surface of the glass. The glass and gel mold the phase into a hemisphere; (middle) as the phase grows, it compacts the gel until, in a kind of fracture, it pushes the gel away from the glass. As the phase grows, it is molded by the fracture forming into a "fried egg". As the phase matures, the white becomes more crystalline than the yolk; and (bottom) later in the egg's maturation, the yolks also become more crystalline. (top–bottom) As the fried eggs grow, the whites and yolks contain similar amounts of Mg^{2+} and likely occlude parts of the gel that are strong enough to resist the crystallization pressure.

decreases in supersaturations and an increase in the ratio of Mg^{2+} to Ca^{2+} ions over time. We further speculate that the maturation rates between the yolks and whites are related to differences in their surface-to-volume ratios, with the whites having a higher surface-to-volume ratio than the yolks when interacting with the solution.

Based on our findings and the literature, we propose the following explanation of how the fried egg-like crystals form (Fig. 6). Diffusion of calcium, magnesium, and carbonate ions into the diffusion cell results in a Mg-calcium carbonate phase nucleating on the glass substrate. The crystals may begin as an amorphous phase, as an amorphous phase would take on a hemispherical shape confined between the stiff glass and compliant gel (Fig. 4g (white arrows)). Further, ACC can incorporate large amounts of magnesium, which upon crystallization, results in Mg-containing calcite (Fig. S8). At some point, the "fried eggs" evolve via a crystal nucleation event followed by a non-crystallographic branching or split growth process [25–27,32]. As the crystals grow, they exert a crystallization pressure, P_{cryst}, on their surroundings [58]. Note: in our system, P_{cryst} is comparable to the elastic modulus of the gel [45], such that stresses exerted by the gel should be strong enough to hinder crystal growth. Therefore, the easiest route for the crystals to grow is along the gel-glass interface. Thus, in a kind of fracture, the crystals delaminate the gel from the glass and are "molded" by the resultant anisotropic interstitial space. As the crystals grow, they likely occlude those parts of the gel network that are strong enough to resist the P_{cryst} exerted by the crystals forming into composites [36,37,45].

5. Conclusion

We have developed a biologically-inspired strategy for chemo-mechanically influencing the growth of crystals. Precipitation of calcium carbonate in diffusion cells containing Mg^{2+} ions and mechanically strong gels resulted in the formation of Mg-calcite crystals with fried egg-like morphologies. In contrast, precipitation within cells containing only Mg^{2+} or gels resulted in aragonite spheroids or "squished" calcite crystals with rhombohedral features, respectively. Investigation of the "fried eggs" over time revealed that they start as egg yolks (or hemispheres) and the whites form later; and that the Mg-calcite forming the fried egg-like structures becomes more crystalline over time, and the "egg whites" make this transition before the "yolks". We propose that the "fried eggs" form due to a spherulitic growth process molded by the delamination of the compliant gel from the stiff glass slide. We envisage that diffusion setups allowing the real-time monitoring of crystal growth [59] will provide additional insights into the formation of calcium carbonate phases under the combined chemo-mechanical influence of Mg^{2+} ions and mechanically strong gels. Further, we can expand the presented strategy to a broad range of crystals and gels with tailored functional properties [60–62]. Such studies will provide a deeper understanding of biomineralization and platforms for controllably forming synthetic crystals with unique functional properties for applications in photonics [63], construction [64], and others.

6. Materials and methods

6.1. Diffusion cell

The diffusion cells were constructed from two glass slides sandwiching a gel film (~2 mm thick; Fig. 1, left). Before construction, the glass slides were cut into pieces (25 × 25 mm), sonicated in acetone for 5 min and plasma cleaned in air for 5 min to remove any impurities from their surface. The gel films were produced from agarose Type IB at 3% w/v (AIB3; Sigma-Aldrich) and at a 4% w/v (AIB4), and from agarose Type IX at 3% w/v (AIX3; Sigma-Aldrich). Agarose solutions were prepared by dissolving agarose powder in hot deionized (DI) water (18.2 MΩ cm^{-1}, Barnstead Easypure RoDI). The solutions were poured into polystyrene Petri dishes (100 × 20 mm), resulting in films approximately 2 mm thick. The AIB films were cooled in the Petri dishes at room temperature, and the AIX3 films were cooled in the Petri dishes in a refrigerator (8 ± 2 °C) for 30 min. Next, the films were removed from the Petri dishes and cut into pieces (21 × 25 mm). Individual gel pieces were then sandwiched between two glass slides, such that two opposite sides of a gel were flush with two opposite edges of the slides, and two sides were recessed. Finally, the recessed sides were sealed with an adhesive sealant (RTV108, Momentive Performance Materials Inc.), completing the diffusion cell. Control cells were constructed without gel and with hydrophobic glass slides coated with OTS. OTS slides were produced by coating glass slides with a silane solution (10 mM) of trichloro(octadecyl)silane (≥90%, Sigma-Aldrich) mixed with hexane (95%, Sigma-Aldrich). The silane and hexane were mixed in a glove box with O_2 below 10 ppm and H_2O below 1 ppm and applied to glass slides in a container sealed with parafilm in a glove box. After sitting for 24 h at room temperature, the slides were sonicated in fresh acetone for 5 min and blow-dried with N_2.

6.2. Crystal growth

Crystal growth was conducted in the diffusion cells by solution-based double diffusion (Fig. 1, right). One of the open mouths of the diffusion cells was connected to an aperture in the inner carbonate reservoir and sealed with an adhesive (see above), while the other mouth was submerged within the outer reservoir (Fig. 1, left). The inner reservoir contained a 50 mM solution of sodium bicarbonate (~750 mL, $NaHCO_3$, Sigma-Aldrich, in DI water), and the outer reservoir contained a 50 mM solution of calcium chloride (1.5 L, $CaCl_2{\cdot}2H_2O$, Sigma-Aldrich, in DI water) or 50 mM solution of calcium chloride plus 200 mM magnesium chloride (1.5 L, $MgCl_2{\cdot}6H_2O$, Sigma-Aldrich, in DI water). The experimental setup for cells containing no gel was much the same; however, the upper mouth of the diffusion cells was sealed with scotch tape and the two reservoirs were filled with the solutions. Diffusion was initiated between the reservoirs by carefully removing the tape. The experiments were conducted at room temperature (25 °C) for up to 14 days. At the end of the experiment, the diffusion cells were disconnected from the reservoirs. The gels were then carefully peeled away from the glass slides, and the crystals on the slides were rinsed with DI water and quenched with ethanol. Each crystal growth experiment was conducted in duplicate.

6.3. Gel characterization

The storage modulus, G′, and loss modulus, G″, of the AIX3 and AIB3 gels were measured using a rheometer (Discovery Hybrid Rheometer HR3, TA Instruments) equipped with a 20 mm parallel plate geometry. Samples were prepared by punching a ~20 mm disc from the 2 mm thick sheets of gel. 220 grit PSA-backed sandpaper was attached to upper and lower plates to prevent slippage during testing, and a small amount of DI water was added at the sample edge to prevent dehydration. Dynamic oscillatory strain sweep measurements, from 0.01 to 100% strain, were performed on the gel discs at a frequency of 1 Hz at 25 °C (Fig. S1). G′ and G″ are plotted against shear strain. G′ is reported as the average of all values in the linear viscoelastic region, and G''_{max} as the maximum value of G″.

6.4. Crystal characterization.

Crystals formed on the slides were examined by plane-polarized light microscopy (Leica NM EP) to determine their morphology and distribution on the glass slides and through crossed-polarizers to determine their optical character. Raman spectra were obtained for the crystals formed on the glass slides, geological calcite (Iceland spar, Ward's Scientific), and crystals from the calcite prismatic and aragonite nacreous layers from the shell of *Atrina rigida* by confocal Raman microscopy (Renishaw InVia, equipped with a RenCam CCD detector) through a 50× long-working-distance objective (Leica Microsystems). Spectra

were acquired with a 488 nm laser for 10 s at 10 mW, over a range of 100–1600 cm^{-1}, at a resolution of 1 cm^{-1}, and were the average of 10 scans. Images were taken of the crystals before the spectra were collected. The crystals were also imaged via SEM (Zeiss Gemini 500), utilizing an InLense high-efficiency secondary electron (HE-SE2) detector at an accelerating voltage of 3 kV and a working distance of ~6 mm. Before imaging, the slides were sputter-coated with either Ir or Au/Pd at 30 mA for 20 s. EDS data was obtained with an Ultim Max detector (Oxford X-ray detection system, Aztec EDS). Point spectra were acquired at an accelerating voltage of 10 kV, a working distance of 6–7 mm, and an acquisition time of 2–4 min. For each "fried egg", 6-point spectra (three points in the "yolk" and three in the "whites") were acquired for five representative "eggs" at each time point (Day 5, 9, and 14).

6.5. Raman data processing

Spectra were background-subtracted using the "subtract background" function in WiRE 4.2 (Renishaw plc., Wotton-under-Edge, UK). Spectra were then imported into Igor Pro 7 (WaveMetrics, Inc, Lake Oswego, OR, USA), where the spectra were analyzed and plots generated. The x (wavenumber) and y (intensity) data were imported and converted to waveform data (in which the x values are evenly spaced). Spectra were excluded from the analysis if: 1) The signal-to-noise ratio was <50 (where the signal was calculated as the maximum intensity of the ν_1 carbonate peak and the noise was calculated as the standard deviation of the intensity between the featureless spectral region of 1520–1580 cm^{-1}); 2) The area of the characteristic glass envelope (500–650 cm^{-1}, with a local linear background subtraction) divided by the intensity of the carbonate ν_1 peak was greater than 5; and 3) There was a strong fluorescence background inhibiting a reliable background subtraction. After the exclusion process, spectra were cropped to the 105–1280 cm^{-1} region, and, using a glass spectrum obtained during the Raman data acquisition, glass was manually subtracted from each calcium carbonate spectrum. The FWHM of the carbonate ν_1 peak was then calculated for each spectrum. Next, the peak position values (Fig. S6c) were approximated by fitting the peaks with a Lorentzian function using the Igor Pro Multipeak Fitting Tool. Finally, the peak position and width values were exported for statistical analysis.

6.6. Statistical analysis

All statistical analyses and plots were performed and generated using JMP® (Version 16.0.0. SAS Institute Inc., Cary, NC, 1989–2021). For the calcite crystals with "fried egg" morphologies, multiple points were acquired across the whites of some individual eggs. These points were treated as technical replicates and averaged before analysis. When comparing two groups (Fig. S5 and Fig. S6), p values were determined using the independent samples t-test. Before these comparisons, data acquired from the same individual crystal ("white" and "yolk") were averaged. For Fig. 4, a linear mixed-effects model was used to analyze FWHM with the fixed effects of spot location (yolk vs. white), time of maturation (5, 9, or 14 days), and the interaction of maturation time and location of the spot. Because some eggs had measurements at both locations (white and yolk), an individual egg identifier was added as a random effect. Fixed effects were tested using F tests, and post hoc pairwise comparisons were performed using Tukey's honestly significant difference test. Where appropriate, box plots overlay the data.

CRediT authorship contribution statement

Damian Palin: Conceptualization, Methodology, Formal analysis, Investigation, Resources, Writing – original draft, Visualization, Supervision, Project administration, Funding acquisition. **Jennie A.M.R. Kunitake:** Formal analysis, Investigation, Data curation, Writing – review & editing, Visualization, Supervision. **Marina P. Chang:** Methodology, Investigation, Writing – review & editing. **Stephan Sutter:** Formal analysis, Investigation, Writing – review & editing, Visualization. **Lara A. Estroff:** Conceptualization, Methodology, Resources, Writing – review & editing, Supervision, Project administration, Funding acquisition.

Declaration of Competing Interest

The authors declare that they have no known competing financial interests or personal relationships that could have appeared to influence the work reported in this paper.

Data availability

Data will be made available on request.

Acknowledgement

This project has received funding from the European Union's Framework Horizon 2020 research and innovation programme under the Marie Sklodowska-Curie Grant Agreement No. 747736 and Cornell's Engineering Learning Initiatives (ELI). It also made use of the Cornell Center for Materials Research (CCMR) Shared Facilities, supported through the NSF MRSEC program (DMR-1719875), and partial support came from the U.S. Department of Energy (DOE), Basic Energy Sciences (BES), under award DE-SC0010560. In addition, the authors thank Jiazhen Xu for preparing OTS coated glass slides, Philip Carubia and Dr. Malcolm Thomas in the CCMR for their support in collecting the data, and Dr. Lynn Marie Johnson of the Cornell Statistical Consulting Unit for her helpful input.

Appendix A. Supplementary data

Supplementary data to this article can be found online at https://doi.org/10.1016/j.jcrysgro.2022.126943.

References

[1] S. Raz, P.C. Hamilton, F.H. Wilt, S. Weiner, L. Addadi, The transient phase of amorphous calcium carbonate in sea urchin larval spicules: the involvement of proteins and magnesium ions in its formation and stabilization, Adv. Funct. Mater. 13 (6) (2003) 480–486.
[2] Y. Politi, T. Arad, E. Klein, S. Weiner, L. Addadi, Sea urchin spine calcite forms via a transient amorphous calcium carbonate phase, Science 306 (5699) (2004) 1161–1164.
[3] J. Seto, Y. Ma, S.A. Davis, F. Meldrum, A. Gourrier, Y.-Y. Kim, U. Schilde, M. Sztucki, M. Burghammer, S. Maltsev, C. Jäger, Structure-property relationships of a biological mesocrystal in the adult sea urchin spine, Proc. Natl. Acad. Sci. 109 (10) (2012) 3699–3704.
[4] J.C. Weaver, G.W. Milliron, A. Miserez, K. Evans-Lutterodt, S. Herrera, I. Gallana, W.J. Mershon, B. Swanson, P. Zavattieri, E. DiMasi, D. Kisailus, The stomatopod dactyl club: a formidable damage-tolerant biological hammer, Science 336 (6086) (2012) 1275–1280.
[5] S. Amini, M. Tadayon, S. Idapalapati, A. Miserez, The role of quasi-plasticity in the extreme contact damage tolerance of the stomatopod dactyl club, Nat. Mater. 14 (9) (2015) 943–950.
[6] I. Polishchuk, A.A. Bracha, L. Bloch, D. Levy, S. Kozachkevich, Y. Etinger-Geller, Y. Kauffmann, M. Burghammer, C. Giacobbe, J. Villanova, G. Hendler, C.-Y. Sun, A. J. Giuffre, M.A. Marcus, L. Kundanati, P. Zalansky, N.M. Pugno, P.U.P.A. Gilbert, A. Katsman, B. Pokroy, Coherently aligned nanoparticles within a biogenic single crystal: a biological prestressing strategy, Science 358 (6368) (2017) 1294–1298.
[7] E. Beniash, J. Aizenberg, L. Addadi, S. Weiner, Amorphous calcium carbonate transforms into calcite during sea urchin larval spicule growth, Proc. R. Soc. Lond. B 264 (1997) 461–465.
[8] J. Gim, N. Schnitzer, L.M. Otter, Y. Cui, S. Motreuil, F. Marin, S.E. Wolf, D.E. Jacob, A. Misra, R. Hovden, Nanoscale deformation mechanics reveal resilience in nacre of Pinna nobilis shell, Nat. Commun. 10 (1) (2019), 4822.
[9] J. Aizenberg, A. Tkachenko, S. Weiner, L. Addadi, G. Hendler, Calcitic microlenses as part of the photoreceptor system in brittlestars, Nature 412 (6849) (2001) 819–822.
[10] L. Li, M.J. Connors, M. Kolle, G.T. England, D.I. Speiser, X. Xiao, J. Aizenberg, C. Ortiz, Multifunctionality of chiton biomineralized armor with an integrated visual system, Science 350 (6263) (2015) 952–956.
[11] P. Harting, On the artificial production of some of the principal organic calcareous formations, J. Microsc. Sci. 20 (1872) 118–123.
[12] S. Leduc, La biologie synthétique; Etudes de biophysique, A. Poinat, Paris, 1912.

[13] F.D. Miles, The apparent hemihedrism of crystals of lead chloride and some other salts, Proc. R. Soc. Lond., A 132 (819) (1931) 266–281.
[14] A.A. Chernov. Modern Crystallography III: Crystal Growth, Springer Series in Solid State Sciences, Springer-Verlag, Berlin, Heidelberg, New York, Tokyo, 1984.
[15] Y. Kitano, The behavior of various inorganic ions in the separation of calcium carbonate from a bicarbonate solution, Bull. Chem. Soc. Jpn. 35 (12) (1962) 1973–1980.
[16] F. Lippmann, in: Sedimentary Carbonate Minerals 6, Springer Berlin Heidelberg, New York, Heidelberg, Berlin, 1973.
[17] M.M. Reddy, G.H. Nancollas, The crystallization of calcium carbonate: IV. The effect of magnesium, strontium and sulfate ions, J. Cryst. Growth 35 (1) (1976) 33–38.
[18] A. Berman, L. Addadi, S. Weiner, Interactions of sea-urchin skeleton macromolecules with growing calcite crystals—a study of intracrystalline proteins, Nature 331 (6156) (1988) 546–548.
[19] S.L. Tracy, D.A. Williams, H.M. Jennings, The growth of calcite spherulites from solution: II. Kinetics of formation, J. Cryst. Growth 193 (3) (1998) 382–388.
[20] S. Raz, S. Weiner, L. Addadi, Formation of high-magnesian calcites via an amorphous precursor phase: possible biological implications, Adv. Mater. 12 (1) (2000) 38–42.
[21] C.A. Orme, A. Noy, A. Wierzbicki, M.T. McBride, M. Grantham, H.H. Teng, P. M. Dove, J.J. DeYoreo, Formation of chiral morphologies through selective binding of amino acids to calcite surface steps, Nature 411 (6839) (2001) 775–779.
[22] E. Loste, R.M. Wilson, R. Seshadri, F.C. Meldrum, The role of magnesium in stabilising amorphous calcium carbonate and controlling calcite morphologies, J. Cryst. Growth 254 (1–2) (2003) 206–218.
[23] Z. Liu, Z. Zhang, Z. Wang, B. Jin, D. Li, J. Tao, R. Tang, J.J. De Yoreo, Shape-preserving amorphous-to-crystalline transformation of $CaCO_3$ revealed by in situ TEM, Proc. Natl. Acad. Sci. 117 (7) (2020) 3397–3404.
[24] C. Tsao, P.-T. Yu, S.-L. Li, I.-J. Hsu, Y.-C. Chuang, C.-K. Chang, S.-J. Chen, J.C. C. Chan, Ambient formation of spherulites of Mg-calcite in an aqueous lipid solution through the interplay between multiple pathways, J. Phys. Chem. C 124 (2020) 20538–20546.
[25] H.D. Keith, F.J. Padden Jr., A phenomenological theory of spherulitic crystallization, J. Appl. Phys. 34 (8) (1963) 2409–2421.
[26] N. Goldenfeld, Theory of spherulitic crystallization, J. Cryst. Growth 84 (4) (1987) 601–608.
[27] A.G. Shtukenberg, Y.O. Punin, E. Gunn, B. Kahr, Spherulites, Chem. Rev. 112 (3) (2012) 1805–1838.
[28] M.M. Reddy, Calcium carbonate nucleation and crystal growth in dilute aqueous solutions at 25oC, U.S. Geol. Surv. Bull. (1578) (1986) 169–182.
[29] A. Gutjahr, H. Dabringhaus, R. Lacmann, Studies of the growth and dissolution kinetics of the $CaCO_3$ polymorphs calcite and aragonite II. The influence of divalent cation additives on the growth and dissolution rates, J. Cryst. Growth 158 (3) (1996) 310–315.
[30] R. Berner, The role of magnesium in the crystal growth of calcite and aragonite from sea water, Geochim. Cosmochim. Acta 39 (4) (1975) 489–504.
[31] K.J. Davis, P.M. Dove, J.J. De Yoreo, The role of Mg^{2+} as an impurity in calcite growth, Science 290 (5494) (2000) 1134–1137.
[32] F. Nindiyasari, E. Griesshaber, L. Fernandez-Diaz, J.M. Astilleros, N. Sanchez-Pastor, A. Ziegler, W.W. Schmahl, Effects of Mg and hydrogel solid content on the crystallization of calcium carbonate in biomimetic counter-diffusion systems, Cryst. Growth Des. 14 (9) (2014) 4790–4802.
[33] R.J. Park, F.C. Meldrum, Synthesis of single crystals of calcite with complex morphologies, Adv. Mater. 14 (16) (2002) 1167–1169.
[34] A.S. Finnemore, M.R.J. Scherer, R. Langford, S. Mahajan, S. Ludwigs, F. C. Meldrum, U. Steiner, Nanostructured calcite single crystals with gyroid morphologies, Adv. Mater. 21 (38–39) (2009) 3928–3932.
[35] J.-M. Ha, J.H. Wolf, M.A. Hillmyer, M.D. Ward, Polymorph selectivity under nanoscopic confinement, J. Am. Chem. Soc. 126 (11) (2004) 3382–3383.
[36] E. Asenath-Smith, H. Li, E.C. Keene, Z.W. Seh, L.A. Estroff, Crystal growth of calcium carbonate in hydrogels as a model of biomineralization, Adv. Funct. Mater. 22 (14) (2012) 2891–2914.
[37] H. Li, L.A. Estroff, Calcite growth in hydrogels: assessing the mechanism of polymer-network incorporation into single crystals, Adv. Mater. 21 (4) (2009) 470–473.
[38] J.W. McCauley, R. Roy, Controlled nucleation and crystal growth of various $CaCO_3$ phases by the silica gel technique, Am. Mineral.: Int. J. Earth Planetary Mater. 59 (9–10) (1974) 947–963.
[39] L. Fernandez-Diaz, A. Putnis, M. Prieto, C.V. Putnis, The role of magnesium in the crystallization of calcite and aragonite in a porous medium, J. Sediment. Res. 66 (3) (1996) 482–491.
[40] G. Falini, S. Fermani, M. Gazzano, A. Ripamonti, Biomimetic crystallization of calcium carbonate polymorphs by means of collagenous matrices, Chem. A Eur. J. 3 (11) (1997) 1807–1814.
[41] F. Nudelman, K. Pieterse, A. George, P.H.H. Bomans, H. Friedrich, L.J. Brylka, P.A. J. Hilbers, G. de With, N.A.J.M. Sommerdijk, The role of collagen in bone apatite formation in the presence of hydroxyapatite nucleation inhibitors, Nat. Mater. 9 (12) (2010) 1004–1009.
[42] E.C. Keene, J.S. Evans, L.A. Estroff, Silk fibroin hydrogels coupled with the n16N−β-chitin complex: an in vitro organic matrix for controlling calcium carbonate mineralization, Cryst. Growth Des. 10 (12) (2010) 5169–5175.
[43] M. Sancho-Tomás, S. Fermani, M.A. Durán-Olivencia, F. Otálora, J. Gómez-Morales, G. Falini, J.M. García-Ruiz, Influence of charged polypeptides on nucleation and growth of $CaCO_3$ evaluated by counterdiffusion experiments, Cryst. Growth Des. 13 (9) (2013) 3884–3891.
[44] F. Nindiyasari, A. Ziegler, E. Griesshaber, L. Fernández-Díaz, J. Huber, P. Walther, W.W. Schmahl, Effect of hydrogel matrices on calcite crystal growth morphology, aggregate formation, and co-orientation in biomimetic experiments and biomineralization environments, Cryst. Growth Des. 15 (6) (2015) 2667–2685.
[45] D. Palin, R.W. Style, J. Zlopaša, J.J. Petrozzini, M.A. Pfeifer, H.M. Jonkers, E. R. Dufresne, L.A. Estroff, Forming anisotropic crystal composites: assessing the mechanical translation of gel network anisotropy to calcite crystal form, J. Am. Chem. Soc. 143 (9) (2021) 3439–3447.
[46] A.A. Chernov, D.E. Temkin, A.M. Melnikova, Theory of solid inclusions capture during crystal-growth from a melt, Kristallografiya 21 (4) (1976) 652–660.
[47] S. Bhagavantam, T. Venkatarayudu, Raman effect in relation to crystal structure, Proc. Indian Acad. Sci. 9 (3) (1939) 224–258.
[48] S.P.S. Porto, J.A. Giordmaine, T.C. Damen, Depolarization of Raman scattering in calcite, Phys. Rev. 147 (2) (1966) 608–611.
[49] W.D. Bischoff, S.K. Sharma, F.T. MacKenzie, Carbonate ion disorder in synthetic and biogenic magnesian calcites: a Raman spectral study, Am. Mineral. 70 (5–6) (1985) 581–589.
[50] E.E. Coleyshaw, G. Crump, W.P. Griffith, Vibrational spectra of the hydrated carbonate minerals ikaite, monohydrocalcite, lansfordite and nesquehonite, Spectrochim. Acta Part A: Mol. Biomol. Spectrosc. 59 (10) (2003) 2231–2239.
[51] K. Kim, I.S. Lee, A. Centrone, T.A. Hatton, A.S. Myerson, Formation of nanosized organic molecular crystals on engineered surfaces, J. Am. Chem. Soc. 131 (51) (2009) 18212–18213.
[52] S.Y. Bahn, B.H. Jo, Y.S. Choi, H.J. Cha, Control of nacre biomineralization by Pif80 in pearl oyster, Sci. Adv. 3 (8) (2017) e1700765.
[53] J. Perrin, D. Vielzeuf, D. Laporte, A. Ricolleau, G.R. Rossman, N. Floquet, Raman characterization of synthetic magnesian calcites, Am. Mineral. 101 (11) (2016) 2525–2538.
[54] J. Ihli, W.C. Wong, E.H. Noel, Y.-Y. Kim, A.N. Kulak, H.K. Christenson, M.J. Duer, F.C. Meldrum, Dehydration and crystallization of amorphous calcium carbonate in solution and in air, Nat. Commun. 5 (1) (2014), 3169.
[55] A. Putnis, Why mineral interfaces matter, Science 343 (6178) (2014) 1441–1442.
[56] A. Gal, W. Habraken, D. Gur, P. Fratzl, S. Weiner, L. Addadi, Calcite crystal growth by a solid-state transformation of stabilized amorphous calcium carbonate nanospheres in a hydrogel, Angew. Chem. Int. Ed. 52 (18) (2013) 4867–4870.
[57] J.R. Dorvee, A.L. Boskey, L.A. Estroff, Rediscovering hydrogel-based double-diffusion systems for studying biomineralization, CrystEngComm 14 (18) (2012) 5681–5700.
[58] L.A. Rijniers, H.P. Huinink, L. Pel, K. Kopinga, Experimental evidence of crystallization pressure inside porous media, Phys. Rev. Lett. 94 (7) (2005), 075503.
[59] G. Zhang, C. Verdugo-Escamilla, D. Choquesillo-Lazarte, J.M. García-Ruiz, Thermal assisted self-organization of calcium carbonate, Nat. Commun. 9 (1) (2018), 5221.
[60] E.S. Place, N.D. Evans, M.M. Stevens, Complexity in biomaterials for tissue engineering, Nat. Mater. 8 (6) (2009) 457–470.
[61] M. Bechthold, J.C. Weaver, Materials science and architecture, Nat. Rev. Mater. 2 (12) (2017) 1–19.
[62] C.M. Soukoulis, M. Wegener, Past achievements and future challenges in the development of three-dimensional photonic metamaterials, Nat. Photonics 5 (9) (2011) 523–530.
[63] M.T. Lloyd, A.C. Mayer, S. Subramanian, D.A. Mourey, D.J. Herman, A.V. Bapat, J. E. Anthony, G.G. Malliaras, Efficient solution-processed photovoltaic cells based on an anthradithiophene/fullerene blend, J. Am. Chem. Soc. 129 (29) (2007) 9144–9149.
[64] D. Palin, V. Wiktor, H.M. Jonkers, A bacteria-based bead for possible self-healing marine concrete applications, Smart Mater. Struct. 25 (8) (2016) 84008–84013.